Automated virtual reduction of displaced distal radius fractures

AUTOMATED VIRTUAL REDUCTION OF DISPLACED DISTAL RADIUS FRACTURES

J. Osstyn⋆   *F. Danckaers*⋆   *A. Van Haver*°   *J. Oramas*⋆   *M. Vanhees*†   *J. Sijbers*⋆

⋆ imec - Vision Lab & imec - IDLab, University of Antwerp, Antwerp, Belgium
† Department of Orthopedic Surgery, AZ Monica Hospital and Antwerp University Hospital
† ASTARC, University of Antwerp, Antwerp, Belgium
° More Institute, Antwerp, Belgium

ABSTRACT

A distal radius fracture is one of the most common fractures treated in emergency departments. Pre-operative 3D virtual reduction of distal radius fractures is key as it improves the recovery process and reduces complications. Unfortunately, most state-of-the-art virtual reduction methods are either interactive or semi-automatic, which are labour intensive and suffer from high inter-observer variability.

In this work, we propose a fully automated algorithm for the reduction of displaced fractures that is robust to both fracture segmentation errors and large fragment displacements. A strategy is proposed to adaptively select landmarks for fragment replacement and iteratively moving the fragments towards a template extracted from the contralateral radius. Real datasets of distal radius fractures with fragment displacements were used to validate our method. Results show that, in terms of distance to the mirrored contralateral radius, the automated reductions closely resemble the manual reductions by the surgeon.

Index Terms— Distal radius fracture, Pre-operative planning, Fracture reduction

1. INTRODUCTION

A distal radius fracture is one of the most common fractures treated in emergency departments [1]. In the most favorable case (81%), plaster treatment will suffice, but often surgery is required to reconstruct the bone from the displaced parts (19%) [2]. Virtualizing the surgical procedure for preoperative planning improves the accuracy of the surgery, resulting in an improved anatomical bone reconstruction with increased stability [3]. As a result, the recovery time is shortened and the risk of complications is reduced. Algorithms for virtual reduction are therefore highly desirable.

Many fragment repositioning methods described in literature are interactive [4–7] or semiautomatic [7–10]. Irwansyah et al. described Computer-Assisted Fracture Reduction (CAFR), an interactive approach for virtual preoperative planning [6]. CAFR is a 3D simulation tool that allows surgeons to manually relocate fracture fragments, which is however nontrivial as 3D movements have to be controlled by 2D mouse movements. Recently, Irwansyah et al. proposed more implicit interactive approaches, such as paired-point registration [4, 5]. To match two fracture faces, the surgeon indicates several points of interest on one fragment and selects for each of these a corresponding point on the complement fragment. In landmark-based registration, the clinical expert marks specific anatomy locations on the fragment surface and reduces the fragmented bone guided by the contralateral bone [4, 5]. Idram et al. proposed an interactive reduction approach based on the registration of fracture lines, which are extracted from 3D CT-images by manually selecting sequential feature points [4, 5]. While effective, such interactive approaches require full attention of the surgeon and are time-inefficient.

Semi-automatic methods require less frequent and less complex user intervention. Fürnstahl et al. proposed a method that requires manual identification of fragments [8] after which the fragments are separated and registered in an automated way. Luque-Luque et al. described an algorithm that calculates fracture surfaces and only requires the user to select matching fracture patches and set up some parameters for proper identification of the fracture zone [9]. To guide the bone reduction, statistical shape models (SSMs) have been employed. Klíma et al. developed a semi-automatic method that uses an SSM to ensure bone length recovery and as such, to reduce surgical complications [11]. In the strategy proposed by Albrecht et al., first an SSM is fitted to an initial alignment of the fracture fragments, after which the fracture is reduced by finding closest point pairs [12]. Their method is semi-automated in that the length of the original bone has to be estimated by the user.

While semi-automated methods are an improvement over more interactive approaches, they are still error prone and time consuming. Automatic fragment reassembly methods exist, yet they mostly rely on surface identification and -matching based on topology, geometry or surface signature [13–16]. This approach is difficult to apply to bone fracture reduction as there is heterogeneous trabecular tissue beneath the cortical surface, complicating segmentation and preventing high quality reduction of the resulting fragments.

In this paper, we present a new method for automated fracture reduction in the context of distal radius fractures. The proposed method relies on adaptively selecting landmarks for fragment replacement and iteratively moving the fragments towards a template extracted from the contralateral radius. Our automated reduction method is validated on X-ray CT datasets of a real distal radius fracture and compared to manual reductions by an orthopedic surgeon. To the authors' knowledge, this is the first time a workflow for automated reduction of bone fragments is presented.

2. METHODS

2.1. Preprocessing

Starting from bone fragments obtained from segmentation of CT data by the surgeon, preprocessing is often a necessary first step. Indeed, such fragments are characterized by an irregular surface caused by internal trabecular structures. To simplify the computation in the next steps, those structures are removed using Meshlab by exploiting the limited vertex quality of internal structures as de-

scribed in [17]. Next, the surface is smoothed by applying a shrink wrapping algorithm [18]. For each fragment, a sphere is defined that fully encompasses the fragment. This sphere is then iteratively shrunk towards the shape of the fragment, resulting in a relatively smooth fragment surface. Then, region growing is applied to the original fragment to identify the largest region of vertices with similar curvature and normal direction. Such vertices are presumably located on the exterior of the radius and thus corresponding to a point on the target surface. In this paper, the mirrored contralateral radius was used as a target surface. Finally, fragments with significantly intertwined trabecular tissue are joined and treated as a single fragment. In what follows, each fragment is registered to the target using a subset of vertices located on the exterior of the radius, unless stated otherwise.

2.2. Coarse initial alignment

The fractured and mirrored contralateral radius are initially not aligned relative to each other. Hence, a course alignment is performed between the source and target surface. First, both the shaft fragment and the contralateral are translated and subsequently rotated such that their centers coincide with the origin, the x-axis passes through their principal axis, and the distal end is located at +x. This provides a general framework to ease future transformations. Next, the optimal transformation is calculated for the shaft fragment only, through Iterative Closest Point (ICP) and a slicing technique (see section 2.3). The shaft transformations are then applied to the complete set of fragments. A coarse fragment alignment is performed through two ICP transformations with a translation along the x-axis in between. The translation ensures that the upperbound along the x-axis of the joined fragment coincides with that of the contralateral radius, which is particularly important for fractures with large fragment displacements towards the shaft. The small fragments are then individually translated towards the center to a limited extent as they are typically torn apart and away from the center. As a stopping condition for these translations, $\frac{|E(s,t)|}{|s|} > 0.3$ is considered, where $|E(s,t)|$ is the number of points of fragment s enclosed in the contralateral radius t, and $|s|$ is the number of vertices of fragment s. Finally, an ICP transformation of the joined fragment is performed with respect to the mirrored contralateral radius.

2.3. Iterative reduction

During the actual reduction each fragment is rigidly transformed in an iterative way. Fragments are iteratively translated and landmark-transformed until a stopping criterion is met or a predefined maximum number of iterations is reached. The maximum number of iterations was set to 7, which proved to be sufficient in most cases. The selection of both the translation and landmark determination method was based on a cost function f that is based on distance and normal direction, as well as on a metric that encourages close correspondence to the contralateral radius. Let $S = \{s_i \mid i = 1, \ldots, n\}$ and $T = \{t_i \mid i = 1, \ldots, n\}$ denote a set of source vertices and the set of corresponding target vertices, respectively. Then, the cost function is defined as

$$f(S,T) = \alpha \sum_i d(s_i, t_i)^2 - \left(\sum_i \mathbf{n}_{s_i} \cdot \mathbf{n}_{t_i} \right)^2 - \beta M_{d_{max}}, \quad (1)$$

where $d(s_i, t_i)$ is the distance between vertices s_i and t_i, $\mathbf{n}_{s_i}$ and $\mathbf{n}_{t_i}$ the surface normals in s_i and t_i, respectively, and $M_{d_{max}}$ is the number of corresponding vertex pairs (s_i, t_i) on a distance less than

or equal to d_{max}, where $d_{max} = 5$, $\alpha = 0.01$ and $\beta = 100$. Every iteration, the cost of the three approaches is calculated. The minimal of these is set as benchmark to the next iteration. The stopping condition is met if the minimal cost in the current iteration did not decrease compared to the benchmark.

The landmarks for the landmark transformation are determined by one of the following approaches:

Constraint Satisfaction Problem (CSP) Landmark selection is bound to the following constraints: first, the n vertices $\{s_1, \cdots, s_n\}$ on the source mesh with the highest curvature are selected. Second, for every source landmark s_i, the corresponding target vertices $\{t_{i1}, \cdots, t_{im_i}\}$ with approximately the same curvature are identified. Third, a Constraint Satisfaction Problem (CSP) is defined as $\langle X, D, C \rangle$, with variables $X = \{s_1, \cdots, s_n\}$, domains $D = \{\{t_{11}, \cdots, t_{1m_1}\}, \cdots, \{t_{n1}, \cdots, t_{nm_n}\}\}$ and constraints $C = \{d(s_i, s_j) \approx d(t_i, t_j) \mid \forall i, j \in \{1, \cdots, n\} : i \neq j\}$, with $d(x_i, x_j)$ the distance between points x_i and x_j. Next, every source vertex s_i is linked to a single target vertex $t_i \in \{t_{i1}, \cdots, t_{im_i}\}$ such that the distances between all pairs of vertices on the source surface are similar to those of the corresponding pairs of vertices on the target surface.

Normal ray comparison In the normal ray approach, a subset of n source vertices is selected from the set of vertices resulting from the preprocessing step. Next, for each of these source vertices, the normal ray is intersected with the target surface. If an intersection is found and the dot product between the normals of the intersection point and source vertex is at least 0.6, the closest vertex to this point is a potential target vertex. In case of multiple qualifying intersection points, the point with the lowest cost, being $d(s_i, t_i)^2 / |\mathbf{n}_{s_i} \cdot \mathbf{n}_{t_i}|$, is chosen.

Fragment slicing In this approach, an Oriented Bounding Box (OBB) is determined around the fragment. For each two opposite sides of the OBB, a series of equally spaced planes parallel to and in between of the two sides is determined. Intersecting these planes with both fragment and mirrored contralateral radius results in two series of 2D lines, which are now source and target in an ICP transformation. The more complex 3D problem is reduced to a layered 2D problem. The landmarks determined during preprocessing are not used in this approach.

For both the CSP and the Normal ray approach, a subset of $n = 50$ vertices was chosen. After successful registration of a fragment, the fragment is joined with the other fragments. This joined fragment is then registered in the same iterative way, after which the fragment registration of the next fragment starts. The developed fragment reduction software was written in Python using VTK [19].

3. EXPERIMENTS

CT images from 25 patients with a distal radius fracture were used to validate our fragment reduction algorithm. The number of fragments per fracture ranges from one up to eight. The fragments as well as the shaft showed highly irregular surfaces for three main reasons. First, the dataset was segmented from bilateral high resolution CT scans of distal radius fractures based on thresholding and manual modifications, using Mimics 24.0 (Materialise, Belgium). This is a challenging task due to the heterogeneous trabecular tissue. Second, the fragments were voxelized, which results in a discretized surface. Finally, the fragments were segmented slice by slice, resulting in (irregular) fragment surfaces. Side- and top-views of four of the radius fragment datasets are shown in Fig. 1.
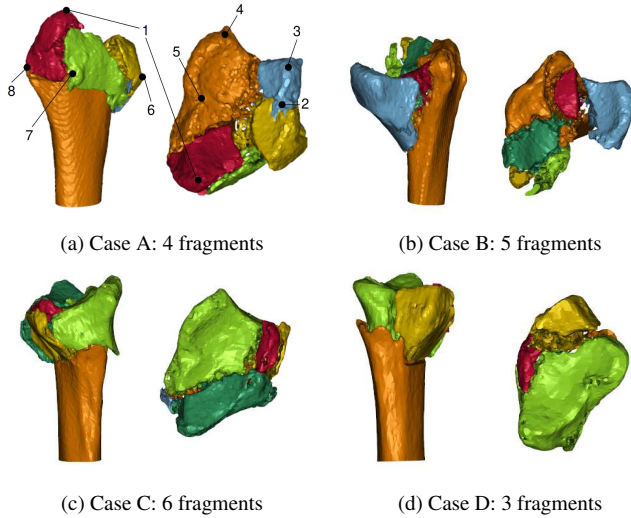
(a) Case A: 4 fragments   (b) Case B: 5 fragments

(c) Case C: 6 fragments   (d) Case D: 3 fragments

Fig. 1: Side-view and top-view for four datasets

4. RESULTS

4.1. Preprocessing and initial alignment

Fig. 2 shows the result after initial alignment of the fragments with the contralateral radius.
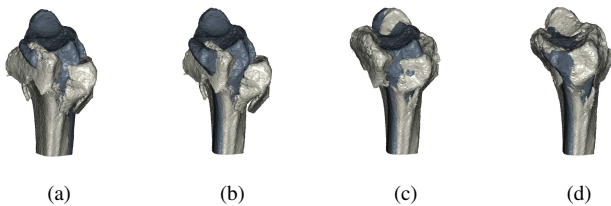

(a)   (b)   (c)   (d)

Fig. 2: Initial fragment alignment. (a) initial situation after transformation to the coordinate system. (b) aligning the shaft with the mirrored contralateral radius. (c) aligning the smaller fragments in line with the shaft. (d) applying small translations to refine the alignment.

4.2. Reduction

4.2.1. Qualitative aspects

For seventeen datasets, the proposed automated reduction closely resembles the corresponding manual reduction by the surgeon. The differences between four of the remaining datasets and the manual reductions could be associated with a difference in shape between the contralateral radius and the shaft, invalidating the use of the contralateral radius as an accurate template for those cases. A length mismatch between contralateral radius and shaft led to an inaccurate template as well for two datasets. For the two remaining datasets, the contralateral radius fitted perfectly to the shaft, however an unreasonable automated reduction was produced.

The distal end is the most important part in a fracture reduction as this supports the functionality and mobility of the wrist. In twenty two cases, the distal end was reconstructed in an anatomically reasonable way with little remaining gaps, while in three cases,

the distal end suffered from level differences between badly reduced fragments.

4.2.2. Quantitative evaluation

In the evaluation of reduction results, the global shape of the reduced bone is key. The shape of the reduction should closely match that of the original radius. Therefore, shrink wrapping was applied to the surgeon's reduction, our reduction and the mirrored contralateral radius. For both our reduction and the surgeon's reduction, the signed distance to the mirrored contralateral radius was calculated. For a surgery of a distal radius fracture, a maximum of 2 mm geometric deviation is accepted for every surface point. On average over all 25 datasets, our reductions had a geometric deviation of less than 2 mm for 87,5% of the vertices on the shrink-wrapped surface. For the surgeon's reduction, this is 82,5%. In only two cases, among which case B from Fig. 1b, the surgeon's reduction had less violations of the 2 mm tolerance as measured by the generated distance maps. We tested whether a one-sided null hypothesis H_0 could be rejected, stating that the percentage of surface points in the surgeon's reductions with a geometric deviation of at most 2 mm was less than or equal to that of our reduction, using a Wilcoxon signed-rank test with significance level 0.05. With a p-value of 0.998, H_0 could not be rejected.

For the four datasets form Fig. 1, two researchers placed independently from each other eight landmarks at well recognizable anatomical locations, on the contralateral bone and the fragments from our reductions and from the surgeon's reductions. Among these landmarks were two important anatomical locations, being the styloid process (landmark 1) and the Lister's tubercle (landmark 6). Subsequently, the distance was measured between the landmarks on the contralateral bone and the corresponding landmarks on both reductions. The measurements showed an error of $(2,4 \pm 1,7)$ mm, with inter-observer variability 1,8 mm for the reductions produced by our algorithm and $(3,5 \pm 1,8)$ mm with inter-observer variability 1,7 mm for the surgeon's reduction.

5. DISCUSSION

In this paper, an algorithm for fragment reduction of the fractured distal radius bone was presented. Our proposed approach is fully automatic and robust to noise introduced by the manual voxelized segmentation. Our algorithm combines the advantages of three sub-algorithms to determine corresponding points and therefore assures that the optimal transformation is performed in every iteration. The current algorithm assumes the availability of the contralateral radius. This can be regarded as a disadvantage. The patient may have broken both wrists, or there may be a significant difference between left and right radius (e.g. due to a previous trauma). Moreover, the patient is exposed to more radiation if both arms are scanned. In future work, we intend to replace the mirrored radius by an SSM and invoke deep learning to improve correspondences or even to carry out the full reduction process [11, 20].

6. CONCLUSION

This paper proposes a fully automatic virtual reduction algorithm for distal radius fractures. The algorithm is subdivided in multiple phases, being preprocessing, coarse initial alignment and iterative reduction. The algorithm was applied on fragment sets from 25 fractured radius cases, leading to promising results. Visualization of the reduced fragments indicate that the automated fragment reduction
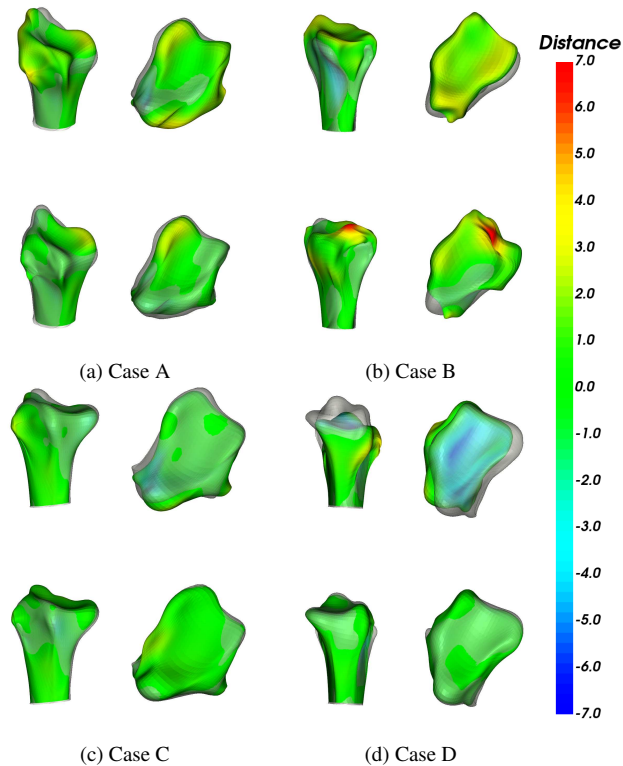
Fig. 3: Distance map for the four datasets shown in Fig. 1, computed from the contralateral bone (shown as grey overlay). Upper row: surgeon's reduction, bottom row: our reduction.

yields plausible results resembling manual reduction by the clinical experts.

7. COMPLIANCE WITH ETHICAL STANDARDS

This study is a part of a larger project, with Belgian registration number B3002020000111, and was reviewed and approved by the ethical committees of the Antwerp University Hospital and the AZ Monica Hospital.

8. ACKNOWLEDGMENTS

9. REFERENCES

[1] S. Meena et al., "Fractures of distal radius: An overview," *Journal of Family Medicine and Primary Care*, vol. 3, pp. 325–32, 2014.

[2] J. Zugasti-Marquínez et al., "Epidemiological study of distal radius fractures in the sanitary area of vigo," *Revista Española de Cirugía Ortopédica y Traumatología*, vol. 66, pp. 38–46, 2022.

[3] C. Zeng et al., "A combination of three-dimensional printing and computer-assisted virtual surgical procedure for preoperative planning of acetabular fracture reduction," *Injury*, vol. 47, pp. 2223–2227, 2016.

[4] I. Irwansyah et al., "Study on repositioning of comminuted fractured bones for computer-aided preoperative planning," *Proceedings of the 2017 4th International Conference on Biomedical and Bioinformatics Engineering*, pp. 30–34, 2017.

[5] I. Irwansyah et al., "Repositioning bone fragments using registration of paired-points and assisted-constraints in virtual bone reduction surgery," *Biomedical Engineering: Applications, Basis and Communications*, vol. 31, pp. 1950021, 2019.

[6] I. Irwansyah et al., "Integration of computer-assisted fracture reduction system and a hybrid 3-DOF-RPS mechanism for assisting the orthopedic surgery," *IOP Conference Series: Materials Science and Engineering*, vol. 308, pp. 012010, 2018.

[7] J. J. Jiménez-Delgado et al., "Computer assisted preoperative planning of bone fracture reduction: Simulation techniques and new trends," *Medical Image Analysis*, vol. 30, pp. 30–45, 2016.

[8] P. Fürnstahl et al., "Computer assisted reconstruction of complex proximal humerus fractures for preoperative planning," *Medical Image Analysis*, vol. 16, no. 3, pp. 704–720, 2012, Computer Assisted Interventions.

[9] A. Luque-Luque et al., "Complex fracture reduction by exact identification of the fracture zone," *Medical Image Analysis*, vol. 72, pp. 102120, 2021.

[10] F. Paulano-Godino and J. J. Jiménez-Delgado, "Identification of fracture zones and its application in automatic bone fracture reduction," *Computer Methods and Programs in Biomedicine*, vol. 141, pp. 93–104, 2017.

[11] O. Klíma et al., "Virtual 2d-3d fracture reduction with bone length recovery using statistical shape models," in *Shape in Medical Imaging*, Cham, 2018, pp. 207–219, Springer International Publishing.

[12] T. Albrecht and T. Vetter, "Automatic fracture reduction," *Lecture Notes in Computer Science*, vol. 7599, pp. 22–29, 2012.

[13] Q. Huang et al., "Reassembling fractured objects by geometric matching," *ACM Trans. Graph.*, vol. 25, pp. 569–578, 2006.

[14] A. Alzaid and S. Dogramadzi, "Reassembly of fractured object using fragment topology," in *10th International Conference on Pattern Recognition Systems (ICPRS-2019)*, 2019, pp. 98–105.

[15] P. Mavridis et al., "Fractured object reassembly via robust surface registration," in *EG 2015 - Short Papers*, 2015.

[16] A. Kronman and L. Joskowicz, "Automatic bone fracture reduction by fracture contact surface identification and registration," *IEEE International Symposium on Biomedical Imaging: from nano to macro*, pp. 246–249, 2013.

[17] F. Osti et al., "CT conversion workflow for intraoperative usage of bony models: From DICOM data to 3D printed models," *Applied Sciences*, vol. 9, pp. 708, 2019.

[18] L. Kobbelt et al., "A shrink wrapping approach to remeshing polygonal surfaces," *Computer Graphics Forum*, vol. 18, 1999.

[19] W. Schroeder et al., *The Visualization Toolkit, An Object-Oriented Approach To 3D Graphics*, 2006.

[20] Z. Zhang et al., "Deep learning based point cloud registration: an overview," *Virtual Reality & Intelligent Hardware*, vol. 2, no. 3, pp. 222–246, 2020, 3D Visual Processing and Reconstruction Special Issue.